Linked cluster expansion of the many-body path integral

Anish Bhardwaj[1] and Efstratios Manousakis[1,2]

[1]*Department of Physics and National High Magnetic Field Laboratory, Florida State University, Tallahassee, Florida 32306-4350, USA*

[2]*Department of Physics, University of Athens, Panepistimioupolis, Zografos, 157 84 Athens, Greece*

(Received 29 March 2018; revised manuscript received 18 September 2019; published 27 November 2019)

We develop an approach of calculating the many-body path integral based on the linked cluster expansion method. First, we derive a linked cluster expansion and we give the diagrammatic rules for calculating the free energy and the pair distribution function $g(r)$ as a systematic power-series expansion in the particle density. We also present a structured Padé approximation scheme in the momentum space to determine $g(r)$. The calculated $g(r)$ for distinguishable particles interacting with Lennard-Jones and hard-sphere potential in various attempted schemes of approximation of the diagrammatic series compares very well with the results of path-integral Monte Carlo simulation. Our method is applicable to a wide range of problems of current general interest and may be extended to the case of identical particles and, in particular, to the case of the many-fermion problem.

DOI: 10.1103/PhysRevB.100.174203

I. INTRODUCTION

The established analytical and semianalytical tools of many-body perturbation theory [1–3] and quantum statistical mechanics [4,5] cannot be applied in a straightforward manner in strongly correlated many-body systems. Using the noninteracting Hamiltonian as the unperturbed part, the matrix elements of the perturbation interaction in the noninteracting basis reduce to the Fourier transform of the interaction potential which is infinite in the case of a hard-core potential or Lennard-Jones–type potential. As a result, one has to replace the repulsive short-range core by some type of effective interaction (or the scattering length) [6,7] by summing an infinite set of selected diagrams. However, in such a scheme the subsequent perturbative expansion to include other diagrams can no longer be consistent; namely, there would be diagrams which are included more than once (double counting) or diagrams of the original expansion which are not included at all. A systematic diagrammatic expansion technique would be welcomed which can manage the effects of the short-range hard-core part of these interactions which bring in so many interesting phenomena arising from short-range correlations. Usually, such problems are approached in one of the following ways: (a) we provide a qualitative description of the many-body physics involved in these systems by using simple models where the application of these standard tools [1–3] becomes possible; or (b) we use an approximate scheme, such as the variational approach, without a clear path to add systematic corrections; or (c) we apply purely numerical approaches such as the Monte Carlo method.

The purpose of this paper is to develop a systematic expansion technique where the most important effects of the short-range part of the interaction are accurately included even at the zeroth-order (or low-order) level using an expansion parameter that controls the rate of convergence even in the presence of strong short-range correlations. For completeness, we mention here that a semiclassical expansion in powers of $\hbar$ which was originated by Wigner [8] and subsequently developed by others [9–14] is different from the approach discussed in this paper. The latter consists of the following two parts.

Part A. We begin from the many-body Feynman [15] path integral at finite temperature [4] and then we extend the cluster expansion [16,17] known for classical statistical mechanics to cast the imaginary-time (finite-temperature) path integral into a systematic expansion up to n-body connected diagrams which corresponds to a density expansion up to nth order. Roughly speaking, our approach is the quantum version of the virial expansion for classical systems. The cluster expansion for classical system in conjunction with the hypernetted-chain approach (HNC) [18–24] is very accurate. Ours is a quantum version of the cluster expansion method and the short-range correlations are intrinsically present from the very inception of the series. We derive a diagrammatic series expansion for the free energy and the pair distribution function, and we show how fully disconnected diagrams generated by our expansion do not contribute. Just like the well-known many-body perturbation theory approach [1–3] provides the diagrammatic rules which enable us to carry out a systematic order-by-order expansion, our approach also yields its own "diagrammar" which allows the treatment of interactions with even a singular short-range part. This part of our work has very general applicability and it is the counterpart of many-body perturbation theory, however, appropriate for systems with strong short-range correlations.

Part B. Next, just as in the case of the standard many-body perturbation theory one can carry out systematic order-by-order expansion, the technique presented here allows us to do that. We chose to benchmark the present technique by applying it to problems where one can obtain essentially exact results by the path-integral Monte Carlo (PIMC) method. Namely, we applied it to systems of distinguishable particles interacting with (a) a Lennard-Jones interaction and (b) a hard-sphere type pair interaction. First, we show that there is a systematic improvement by increasing the order of the expansion. Beyond that, we constructed a scheme using Padé

approximants which (i) reproduces the results of the order-by-order expansion up the calculated order, (ii) yields the exact high-temperature limit of the pair distribution function, and (iii) yields its exact low-density limit. The results for the pair distribution function obtained with this extrapolation scheme are in very good agreement with the results of PIMC down to moderately low temperature.

The method of Padé approximants is a standard tool and has already been proved to be effective when studying physical systems like a system of interacting spins [25–27]. Part A of our approach is a semianalytical tool which yields a new expansion scheme which converges relatively fast for hard-core potentials and stands alone. Part B of our approach outlines a particular way to sum the important contribution and it is not expected to be the only way to include the contribution of the most significant diagrams. It can be extended further in the future by implementing other techniques and ideas. For example, there is the diagrammatic Monte Carlo method and we can imagine that it may be adopted to provide a sampling of this new diagrammatic space. This is what we imply with the statement that part A of this work "stands alone." Part B is only used here to demonstrate the efficiency of the approach, not as the only way to go forward. As it is shown in this paper, part A is general and can be also applied to fermions.

Part A of our paper, i.e., the cluster expansion, our derived diagrammatic rules, etc., are directly applicable to the case of identical particles. Our summation method presented in the part B of this paper is generalizable to the case of identical particles and, therefore, it has the potential to be useful as an alternative approach to the treatment of bosonic and fermionic systems. This part is more extensively discussed in Secs. VII and IX of this paper. Lastly, we would like to note that the approach developed in this work is a general method to treat the quantum many-particle problem. Therefore, it can be applied to other systems in diverse areas of physics, such as systems of trapped ultracold atoms, and possibly to the many-nucleon problem [28], i.e., the hypothetical infinite nuclear matter and neutron stars.

The paper is organized as follows. In Sec. II we discuss the many-body path integral and we cast it in a form useful for the application of our method. In Sec. III we develop the cluster expansion of the path integral that describes the quantum mechanical partition function for a system of distinguishable particles. We discuss some generalizations needed to extend the method to systems of identical particles. We give the diagrammatic rules for a systematic inclusion of all the diagrams order by order in the density. In Sec. IV we discuss the cluster expansion of the free energy and in Sec. V that of the pair distribution function. In Sec. VI we present our results of the method viewed as a systematic power series expansion in the density for both the Lennard-Jones system and hard-sphere systems. In addition, we also propose a Padé-approximation scheme which yields very accurate results for the Lennard-Jones system for densities near the equilibrium density of liquid ^{4}He. In Sec. VII we provide some future directions. The implementation of the method has been summarized in Sec. VIII. Last, in Sec. IX we present our conclusions.

II. MANY-BODY PATH INTEGRAL

To build the path-integral cluster expansion formalism we will follow the same procedure that is used in the case of classical cluster expansion. While our goal in this paper is to study the simpler case of distinguishable particles, we first begin by writing the partition function [4] for a system of N interacting identical particles:

$$Z = \frac{1}{N!}\sum_{P}(\pm 1)^{[P]}\int d^3\vec{r}_1 d^3\vec{r}_2 \ldots d^3\vec{r}_N \times \langle \vec{r}_1, \vec{r}_2, \ldots, \vec{r}_N \mid e^{-\beta\hat{H}} \mid \vec{r}_{P1}, \vec{r}_{P2}, \ldots, \vec{r}_{PN}\rangle. \quad (1)$$

Here, the summation over P means a summation over all permutations of particles and the notation $[P]$ denotes the order of the permutation [4]. In the case of bosons, all permutations contribute with a positive sign. In the case of fermions, $(-1)^{[P]}$ is $+1$ or -1 depending on whether the permutation is even or odd. In the positions $(\vec{r}_{P1}, \vec{r}_{P2}, \ldots, \vec{r}_{PN})$ the indices $P1, P2, \ldots, PN$ are the particle indices after permutation P. In this paper we will deal with the general case of an interacting Hamiltonian $\hat{H}$ of the following form:

$$\hat{H} = -\frac{\hbar^2}{2m}\sum_{i}^{N}\nabla_i^2 + \sum_{i<j} v(r_{ij}). \quad (2)$$

Next, we divide the imaginary-time interval $[0, \theta]$ ($\theta \equiv \hbar\beta$) into M slices of size $\delta\tau = \hbar\beta/M$ to write $e^{-\beta\hat{H}} = e^{-\delta\tau\hat{H}/\hbar}e^{-\delta\tau\hat{H}/\hbar}\ldots e^{-\delta\tau\hat{H}/\hbar}$. As usual we insert in-between each pair of these operators the unit operator expressed as a sum over the complete set of many-body position eigenstates and by using the Trotter approximation we can write the partition function as

$$Z = \sum_{P}\frac{(\pm 1)^{[P]}}{N!}\int_{\vec{r}_i(\theta)=\vec{r}_{Pi}(0)}\prod_{n=1}^{N}\prod_{k=0}^{M-1}\frac{d^3\vec{r}_n^{(k)}}{\lambda_{\delta\tau}^3}e^{-S_E}, \quad (3)$$

where

$$S_E = \frac{\delta\tau}{\hbar}\sum_{k=0}^{M-1}\left[\sum_i \frac{m}{2(\delta\tau)^2}r_i^2(kk+1) + \sum_{i<j} v\left(r_{ij}^{(k)}\right)\right], \quad (4)$$

$$\lambda_\tau \equiv (2\pi\hbar\tau/m)^{1/2}, \quad (5)$$

and $r_{ij}^{(k)} = |\vec{r}_i^{(k)} - \vec{r}_j^{(k)}|$ and $r_i(kl) = |\vec{r}_i^{(k)} - \vec{r}_i^{(l)}|$. The constraint $\vec{r}_i(\theta) = \vec{r}_{Pi}(0)$ on the path integral (where $\theta = \hbar\beta$) means that the sum is over all possible N-particle paths which start at positions $(\vec{r}_1(0), \vec{r}_2(0), \ldots, \vec{r}_N(0))$ at imaginary time $\tau = 0$ and after the "lapse" of an imaginary-time interval of $\beta\hbar$ they end up at positions $(\vec{r}_1(\theta) = \vec{r}_{P1}(0), \vec{r}_2(\theta) = \vec{r}_{P2}(0), \ldots, \vec{r}_N(\theta) = \vec{r}_{PN}(0))$ where $P1, P2, \ldots, PN$ are the particle indices after permutation P.

By taking the limit $M \to \infty$, one can obtain the well-known Feynman's path-integral expression

$$Z = \frac{1}{N!}\sum_{P}(-1)^{[P]}\int_{\vec{r}_i(\theta)=\vec{r}_{Pi}(0)}\mathcal{D}\vec{r}_1\mathcal{D}\vec{r}_2\ldots\mathcal{D}\vec{r}_N e^{-S_E}. \quad (6)$$

The Euclidean action in the above path integral is given by

$$S_E = \int_0^{\hbar\beta} \left(\sum_{i=1}^{N} \frac{1}{2} m \dot{\vec{r}}_i^{\,2} + \sum_{i<j} v(r_{ij}(\tau)) \right) d\tau, \tag{7}$$

where $r_{ij}(\tau) = |\vec{r}_i(\tau) - \vec{r}_j(\tau)|$.

However, the Feynman's path-integral expression is only symbolic and, for all practical purposes, we make use of the expression given by Eq. (3). As discussed in the Abstract and in the Introduction of this paper, in this paper we concentrate our attention to the simpler case of distinguishable particles, which corresponds to considering the identity permutation only.

III. CLUSTER EXPANSION OF PARTITION FUNCTION

In this paper we concentrate only on the identity permutation which corresponds to a system of interacting distinguishable particles. This will allow us to test the method by comparison of our results to PIMC which is accurate in this case because of the absence of the sign problem. Since our method is diagrammatic in nature, it can be extended to include diagrams which correspond to particle permutations [29,30]. Therefore, if we can demonstrate that the method works for distinguishable particles, it would be a promising sign for the applicability of the method to the more complex problem of identical particles and in particular the problem of fermions where quantum Monte Carlo (QMC) fails to address it in an exact way. While we consider the case of distinguishable particles, as we describe our method in this paper, when appropriate, we address the generalizations needed in order to include the permutations.

Now, we concentrate on the dimensionless ratio $\frac{Z}{Z_0}$ where Z_0 is the noninteracting partition function, which can be obtained from Eq. (3) by using the free action, obtained from Eq. (4) with $v(r_{ij}^{(k)}) = 0$, and carrying out the Gaussian integrals

$$Z_0 = \frac{1}{N!} \left(\frac{V}{V_\theta} \right)^N, \qquad V_\theta = \lambda_\theta^3, \tag{8}$$

and since λ_θ is the de Broglie thermal wavelength, V_θ is the de Broglie thermal volume. Thus,

$$\frac{Z}{Z_0} = \left(\frac{V_\theta}{V} \right)^N Z. \tag{9}$$

Next, we start the cluster expansion by defining the function $h_{ij}^{(k)}$ as follows:

$$e^{-\frac{\delta\tau}{\hbar} v(r_{ij}^{(k)})} \equiv 1 + h_{ij}^{(k)}, \tag{10}$$

and the function $L_i(kl)$ as follows:

$$L_i(kl) = \frac{1}{\lambda_{\tau_{kl}}^3} e^{-\pi \frac{r_i^2(kl)}{\lambda_{\tau_{kl}}^2}}, \tag{11}$$

$$\tau_{kl} = |k - l| \delta\tau. \tag{12}$$

Using these definitions the partition function can be written as

$$\frac{Z}{Z_0} = \left(\frac{V_\theta}{V} \right)^N \int \prod_{n=1}^{N} \prod_{k=0}^{M-1} d^3 r_n^{(k)} L_n(kk+1) \prod_{l=0}^{M-1} \prod_{i<j} \left(1 + h_{ij}^{(l)}\right). \tag{13}$$

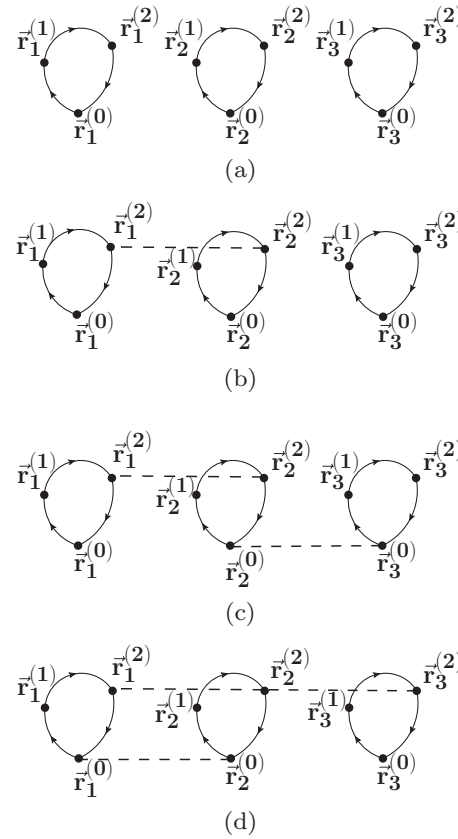

FIG. 1. Few diagrams that appear in the expression for Z when $N = 3$ and $M = 3$.

The expression in Eq. (13) consists of products of $(1 + h_{ij}^{(l))})$, which can be written out as follows:

$$\prod_{l=0}^{M-1} \prod_{i<j} \left(1 + h_{ij}^{(l)}\right) = 1 + \sum_{l=0}^{M-1} \sum_{i<j} h_{ij}^{(l)} + \cdots, \tag{14}$$

where we have omitted terms containing two or more h factors. After substituting the expanded product in Eq. (13) we obtain a sum of integrals. We can keep track of terms by representing each of these integral terms by diagrams. As an example, consider the case of 3 ($N = 3$) particles with 3 time instants ($M = 3$). In this case, the first few terms have been diagrammatically represented in Fig. 1.

We use the following convention for representing such terms:

(1) The positions of the particles at the instants of time which enter in the integral are denoted by solid circles. An integration over these positions is implied.

(2) $h_{ij}^{(k)}$ is denoted by a dashed line labeled by the index (k) (which represents interaction between particles at the same instant of time k) connecting points i and j.

(3) The L function defined by Eq. (11) is denoted by a solid line connecting points $\vec{r}_i^{(k)}$ and $\vec{r}_i^{(l)}$.

(4) Every particle is associated with its own world line, which is made up of products of L functions. The world lines of a pair of particles at a given instant of time can be either disconnected (i.e., there is a factor of unity) or they can be connected by a dashed line.

(5) The world line starts at $\vec{r}_1^{(0)}$ and connects back to $\vec{r}_1^{(0)}$ because of the boundary condition $\vec{r}_i^{(0)} = \vec{r}_i^{(M)}$. Therefore, a world line forms a loop formed by the particle positions at all instants of time.

In the case of identical particles, there are diagrams in which $\vec{r}_i^{(M)} = \vec{r}_{Pi}^{(0)}$, i.e., the particle positions are exchanged at imaginary-time slice M. In this paper, we do not deal with the contribution of such diagrams.

If the world line of a given particle has solid points which are not connected to any other point through dashed lines, then it is possible to perform the integration over those variables exactly by using the following identity:

$$L_i(kl) = \int d^3\vec{r}_i^{(m)} L_i(km) L_i(ml). \tag{15}$$

This result can be interpreted such that the world line now makes a straight connection of the particle coordinate at the initial instant of time, i.e., $\vec{r}_i^{(k)}$ with the particle coordinate at the instant of time 1. This explicit integration removes such intermediate points in our diagrams which are not connected by any dashed line. As an example, consider the diagram in Fig. 1(a). Because of the absence of dashed lines it is possible to perform the integration over all three variables and the diagram equals to unity; similarly, the term in Fig. 1(b) is obtained when the product is such that we have only one dashed line (in this case $h_{12}^{(1)}$); here, particles 1 and 2 are connected but particle 3 is disconnected. Such a term has the following integral form:

$$\left(\frac{V_\theta}{V}\right)^3 \int \prod_{i=1}^{3}\prod_{k=0}^{2} d^3\vec{r}_i^{(k)} L_i(kk+1) h_{12}^{(2)}. \tag{16}$$

The coordinates of particle 3 at all instants of time can be integrated out and, thus, the diagram corresponds to the following expression:

$$\left(\frac{V_\theta}{V}\right)^2 \int \prod_{i=1}^{2}\prod_{k=0}^{2} d^3\vec{r}_i^{(k)} L_i(kk+1) h_{12}^{(2)}. \tag{17}$$

We can further simplify the above expression by noting that the integration over $\vec{r}_1^{(0)}$, $\vec{r}_2^{(0)}$, $\vec{r}_1^{(1)}$, and $\vec{r}_2^{(1)}$ can be performed as these are not connected through a dashed line. The simplification leads to the following term:

$$\left(\frac{V_\theta}{V}\right)^2 \int d^3\vec{r}_1^{(2)} d^3\vec{r}_2^{(2)} L_1(0M) L_2(0M) h_{12}^{(2)} = \frac{1}{V^2} \int d^3\vec{r}_1^{(2)} d^3\vec{r}_2^{(2)} h_{12}^{(2)}. \tag{18}$$

Such a term has been represented in Fig. 2(a). Each of the two L functions corresponding to the world lines of particles 1 and 2 which begin and go back to the same position at zeroth time slice (because $\vec{r}_i^{(M)} = \vec{r}_i^{(0)}$) yield the constant factor $L_i(0M) = 1/V_\theta$. In a similar way, the diagram in Fig. 1(c), which is an example of a connected cluster, can be represented as shown in Fig. 2(b) with a contribution given by

$$\frac{V_\theta}{V^3} \int d^3\vec{r}_1^{(2)} d^3\vec{r}_2^{(2)} d^3\vec{r}_2^{(0)} \;\; d^3\vec{r}_3^{(0)} L_2(02) L_2(20) h_{12}^{(2)} h_{23}^{(0)}. \tag{19}$$

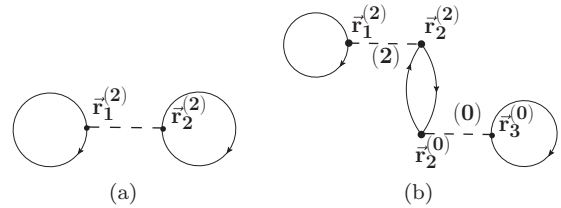

FIG. 2. (a), (b) Show, respectively, simplified versions of the diagrams shown in Figs. 1(b) and in 1(c) after integration over the coordinates of those points which are not connected through h lines to any other point.

A. Diagrammatic rules

Now, let us consider the expansion of Z/Z_0 for a very large number of particles N. In such an expansion we can still have terms which have the same expression as, for example, the diagram of Fig. 2(a) [Eq. (18)], in which the coordinates of all the other particles except 1 and 2 have been integrated out because they were not connected to any other particle by an h line. In addition, the exact same two-body contribution arises when the labels of particles 1 and 2 are interchanged with any of the other $N-2$ particles. Therefore, when we draw a diagram such as the diagram of Fig. 2(a) we imply that we include all the $N(N-1)/2$ diagrams which correspond to those obtained from replacing 1 and 2 with any other pair of particles. Therefore, the contribution of this diagram is going to be

$$\frac{1}{2}(V_\theta \rho)^2 \int d^3\vec{r}_1^{(2)} d^3\vec{r}_2^{(2)} L_1(0M) L_2(0M) h_{12}^{(2)}, \tag{20}$$

where we have used the fact that as $N \to \infty$, $N(N-1)/V^2 \to \rho^2$. To summarize, the expansion of Z/Z_0 can be obtained as a summation of terms which correspond to

$$\frac{Z}{Z_0} = 1 + \sum_{n=2}^{\infty} \sum_{\alpha} D_n^{(\alpha)}, \tag{21}$$

when $D_n^{(\alpha)}$ stands for any n-body diagram. Here, n is the number of particles involved in the diagram and α labels the various n-body diagrams. An n-body diagram is a diagram with n particles connected to each other through dashed lines and each of the remaining $N-n$ particles are not connected to any of the other particles. In this case, the coordinates of the latter $N-n$ particles drop out. To find all $D_n^{(\alpha)}$ we need to draw all topologically distinct n-particle diagrams by following the following rules:

(1) Particle positions are denoted by solid dots labeled $\vec{r}_i^{(k)}$ and they stand for an integration over the coordinate of the ith particle at the kth instant of time.

(2) We need to select the n world lines for each one of the n particles. Each world line starts at time $\tau = 0$ and ends at time $\tau = \hbar\beta$ and it is made out of connected solid lines which correspond to L functions [see Eq. (11)] which connect particle coordinates at intermediate instants of time. The integrations over particle coordinates at intermediate instants of time are allowed unless they are connected to the world line of at least one other particle by a dashed line at the same instant of time.

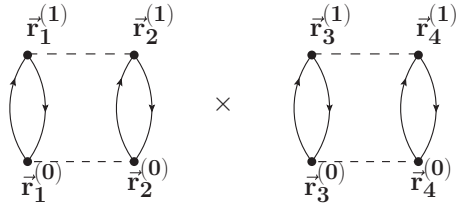

FIG. 3. Example of a disconnected term [see Eq. (22)].

(3) We choose to connect pairs of particle positions $\vec{r}_i^{(k)}$ and $\vec{r}_j^{(k)}$ at the same instant of time k by dashed lines. Each such dashed line labeled as (k) connecting particles i and j gives rise to a factor $h_{ij}^{(k)}$.

(4) For every world line we need to multiply the contribution of the diagram by a *dimensionless* factor of ρV_θ.

(5) The contribution of a diagram is divided by a factor of S, the symmetry factor of the diagram. In the case of the diagram of Fig. 2(a) the factor $\frac{1}{2}$ in Eq. (20) is due to a symmetry factor of 2 due to the fact that by interchanging the two points 1 and 2 the contribution of the diagram remains the same.

B. Connected and disconnected diagrams

An n-body diagram is considered a *connected diagram* when each of the n particles is connected to at least one of the other n particles in the diagram. All the diagrams that appear in Fig. 1 are examples of connected diagrams. On the other hand, we have a disconnected n-body diagram when it is formed out of subsets of particles which are connected in such a way that particles of any given set are connected to each other and they remain disconnected from any particle not belonging to the given set. A simple example (with $M = 2$) of a disconnected term is shown in Fig. 3 and it is given by

$$\left(\frac{V_\theta}{V}\right)^4 \int \prod_{i=1}^{2}\prod_{k=0}^{1} d^3\vec{r}_i^{(k)} L_i(kk+1) h_{12}^{(0)} h_{12}^{(1)} \times \int \prod_{i=3}^{4}\prod_{k=0}^{1} d^3\vec{r}_i^{(k)} L_i(kk+1) h_{34}^{(0)} h_{34}^{(1)}. \quad (22)$$

C. Factorizable diagrams

There are diagrams which can be factorized into products of two or more different diagrams. Consider, for example, the diagram of Fig. 4(a). This diagram is factorizable at the node $\vec{r}_2^{(2)}$ at which point the world line of particle 2 connects via a dynamical h line to the world line of particle 3. This diagram can be written as a product of two parts as illustrated in Fig. 4(b). In order for a diagram to be factorizable, two parts of the diagram should be connected only at a node, namely, a point through which one has to go through when traveling from one part of the diagram to the other part using h lines or L lines.

IV. FREE ENERGY

In the expansion of Z/Z_0 it is possible to regroup the various diagrams in such a way that it can be written as a sum of connected and disconnected clusters. We will use the notation $[i]$ to denote the sum of all connected clusters. It is easy to see that any disconnected cluster can be written in terms of product of connected clusters. We can write the sum of all the diagrams contributing to Z/Z_0 as follows [28]:

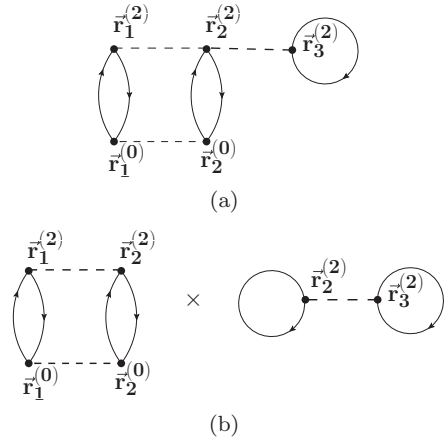

FIG. 4. An example of a factorizable diagram.

$$\frac{Z}{Z_0} = 1 + [i] + \frac{1}{2}[i][j] + \frac{1}{3!}[i][j][k] + \cdots, \quad (23)$$

where $[i]$ denotes the ith connected piece and a summation over $i, j, k, \ldots$ is implied. In addition, the notation $[i][j]$ means a disconnected diagram made out of two parts where no common particle exists. The second term is the sum of all connected diagrams. The third term is the sum of all the disconnected diagrams which are products of just two connected pieces. The factor of $\frac{1}{2}$ is present to avoid double counting of terms in which $[i]$ and $[j]$ are interchanged. Similarly, we have a factor of $\frac{1}{3!}$ in the fourth term which is the sum of all disconnected diagrams made out of three connected pieces.

The free energy $F(N, T, V)$ of the system is obtained as

$$F(N, T, V) = -k_B T N \ln(V/V_\theta) - k_B T \ln\left(\frac{Z}{Z_0}\right). \quad (24)$$

Therefore, the corrections to the ideal gas free energy are given by

$$-\beta\delta F(N, T, V) = \ln\left(\frac{Z}{Z_0}\right). \quad (25)$$

Using the expression in Eq. (23) and the Taylor expansion of $ln(1+x)$ with $x = [i] + \frac{1}{2}[i][j] + \frac{1}{3!}[i][j][k] + \cdots$, we obtain

$$\ln\left(\frac{Z}{Z_0}\right) = [i] + \frac{1}{2}[i][j] + \frac{1}{6}[i][j][k] - \frac{1}{2}[i]\times[j] - \frac{1}{2}[i]\times[j][k] + \frac{1}{3}[i]\times[j]\times[k] + \cdots, \quad (26)$$

and the above expression is correct up to terms which contain less than four disconnected clusters. Using the notation of Ref. [28],

$$[i]\times[j] = [i][j] + \overline{[i][j]} + \overline{\overline{[i][j]}} + \cdots, \quad (27)$$

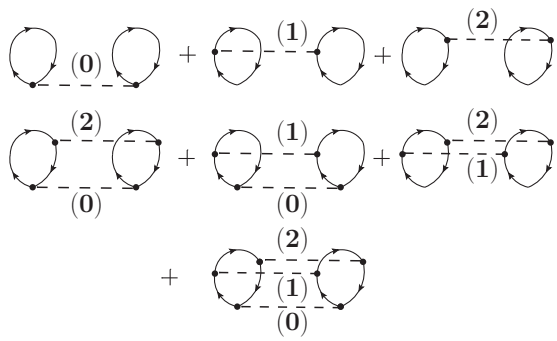

FIG. 5. Diagrams contributing to the free energy which are first order in ρ.

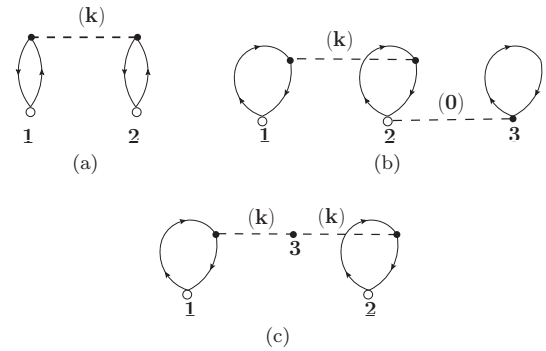

FIG. 6. Examples of diagrams contributing to the numerator of $g(r)$.

where one overhead bar means that the two clusters share one common particle and two such bars imply that they share two particles. Each diagram in $[i]$ is of the order of N and the diagrams contributing to $[i][j]$ are of order of N^2, etc. As a result, the term $[\overline{i][j]}$ is of order N and the term $[\overline{i][j]}$ is of order unity. In general when there is such an overhead bar, it reduces the order of the contribution by a factor N. Substituting Eq. (27) in (26) we obtain the following terms up to order N:

$$-\beta\delta F(N,T,V) = [i] - \frac{1}{2}[\overline{i][j]} + \frac{1}{2}[\overline{i][j][k]} + \frac{1}{3}[\overline{i][j][k]} + \cdots, \tag{28}$$

where $[\overline{i][j][k]}$ means that the three pieces share the same particle. Also, here the ellipses stand for terms containing products of more than three disconnected parts with common particles. Notice that each term is of order N: a disconnected piece is of order N and every overhead line removes a factor of N. As long as each term has just one overhead line less than the number of its disconnected pieces, the contribution of the term is of order N.

We can simplify the above expression by making use of factorizability. We use the notation $[a]$ to denote nonfactorizable type diagram. With this notation $[i]$ can be written as a sum of connected diagrams with all possible factorizable pieces:

$$[i] = [a] + \tfrac{1}{2}[\overline{a\ b}] + \cdots, \tag{29}$$

so that

$$-\beta\delta F(N,T,V) = [a] + \tfrac{1}{2}([\overline{a\ b}] - [\overline{a}][\overline{b}]) + \cdots. \tag{30}$$

Figure 5 shows diagrams contributing to the free energy which are first order in ρ.

V. CLUSTER EXPANSION OF DISTRIBUTION FUNCTION

We now develop a diagrammatic expansion for the pair distribution function. We consider the distinguishable particle case by taking only the identity permutation. The pair distribution function for an isotropic translationally invariant system takes the following form in our notation:

$$g(r) = \frac{\mathcal{N}}{\mathcal{D}},\ \mathcal{D} \equiv \frac{Z}{Z_0}, \tag{31}$$

$$\mathcal{N} \equiv \frac{V}{Z_0}\int \prod_{i=1}^{N}\prod_{k=0}^{M-1} \frac{d^3 r_i^{(k)}}{\Omega_{\delta\tau}} \delta[\vec{r}_{21}(0) - \vec{r}]e^{-S}, \tag{32}$$

where $\Omega_\tau = \lambda_\tau^3$ and Z and Z_0 are the interacting and noninteracting partition functions defined in the previous section. The denominator has been expanded and written in terms of connected and disconnected diagrams as in Eq. (23).

In order to carry out the cluster expansion of the numerator, we need to enrich our diagrammatic notation for the numerator diagrams. Examples of numerator diagrams are shown in Fig. 6. The two open circles labeled as $\vec{r}_1^{(0)}$ and $\vec{r}_2^{(0)}$ represent the external points needed in the expression of the numerator. There are no integrations over these external points and no ρ factors for their world lines. All other diagrammatic elements and rules are identical to those defined in the previous section.

Following Wiringa and Pandharipande [28], let $[I]$ denote the sum over all connected numerator diagrams $[I]$, i.e., diagrams which include points $\vec{r}_1^{(0)}$ and $\vec{r}_2^{(0)}$ as external points. When we carry out the cluster expansion of the numerator we encounter disconnected diagrams with one or more pieces and the total expansion of the numerator can be written as

$$\mathcal{N} = [I] + [I][i] + \tfrac{1}{2}[I][i][j] + \cdots, \tag{33}$$

where a summation over I, i, j, ... is implied. In addition, the notation $[I][i][j]$ means a disconnected diagram made out of three parts where no common particle exists.

Now, we expand the ratio of $\mathcal{N}/\mathcal{D}$ and we obtain

$$\frac{\mathcal{N}}{\mathcal{D}} = [I] + [I][i] - [I]\times[i] + \frac{1}{2}[I][i][j] - \frac{1}{2}[I]\times[i][j] + [I]\times[i]\times[j] - [I][i]\times[j] + \cdots. \tag{34}$$

The following equations yield the product of sums of diagrams which is contained in right-hand side of the above equation:

$$[I]\times[i] = [I][i] + [\overline{I][i]} + \cdots, \tag{35}$$

$$[I]\times[i][j] = [I][i][j] + 2[\overline{I][i]}[j] + [\overline{I][i]}[j] + 2[\overline{I][j]}[i] + \cdots, \tag{36}$$

$$[I]\times[i]\times[j]=[I][i][j]+2\overline{[I][i]}[j]+[I]\overline{[j][i]}+\overline{[I][i][j]}+2\overline{[I]}[\overline{i}][j]+2\overline{[I][i]}[j]+[I]\overline{[i][j]}+\overline{[I][i][j]}+\cdots, \tag{37}$$

$$[I][i]\times[j]=[I][i][j]+\overline{[I][i][j]}+\overline{[I][i]}[j]+[I]\overline{[i][j]}+\overline{[I][i][j]}+[I]\overline{[i]}[j]+\cdots, \tag{38}$$

where $\overline{[I][i][j]}$ means that the three pieces share the same particle. The ellipses stand for more than three disconnected pieces. In addition, the ellipses stand for terms in which the number of common particles is equal to or more than the number of disconnected pieces. These latter terms have been neglected because their contribution relative to that of I vanish in the $N\to\infty$ limit. Using the above equations, we can write the expression given by Eq. (34) as follows:

$$\frac{\mathcal{N}}{\mathcal{D}}=[I]-\overline{[I][i]}+\frac{1}{2}\overline{[I][i][j]}+\overline{[I][i]}[j]+[I]\overline{[i][j]}+\overline{[I][i][j]}+\cdots. \tag{39}$$

We have neglected terms which have the same or more number of overhead lines as the number of disconnected pieces. Again, as long as each term has just one overhead line less than the number of its disconnected pieces, the contribution of the term is of the same order as the order of $[I]$, which is of the order of unity in the case of the distribution function.

We now make use of the factorizability of diagrams to further simplify the above expression. We use the notation $[A]$ to denote a nonfactorizable numerator-type diagram (this contains two external points) and use $[a]$ to denote a nonfactorizable denominator-type diagram. We expand our notation to describe this as follows. The following is an example of a connected diagram $[I_3]$ which has three factorizable pieces

$$[I_3]=\overline{[A\ a_1]}\,\overline{[a_2]}, \tag{40}$$

where the overhead lines denote the points where the diagram $[I_3]$ is factorizable. This means that the sum of the connected diagrams $[I]$ and $[i]$ can be written as follows:

$$[I]=[A]+\overline{[A\ a]}+\overline{[A\ a\ b]}+\frac{1}{2}\overline{[A\ a\ b]}+\tfrac{1}{2}\overline{[A\ a\ b]}+\cdots, \tag{41}$$

$$[i]=[a]+\tfrac{1}{2}\overline{[a\ b]}+\cdots. \tag{42}$$

With this, the final expression for the pair distribution function becomes

$$\frac{\mathcal{N}}{\mathcal{D}}=[A]+\left(\overline{[A\ a]}-\overline{[A]}[a]\right)+\left(\overline{[A\ a\ b]}-\overline{[A\ a]}[b]-[A]\overline{[a\ b]}+\overline{[A]}[a][b]\right)+\left(\frac{1}{2}\overline{[A\ a\ b]}-\overline{[A\ a]}[b]+\frac{1}{2}\overline{[A]}[a][b]\right)+\left(\frac{1}{2}\overline{[A\ a\ b]}-\overline{[A\ a]}[b]-\frac{1}{2}[A]\overline{[a\ b]}+\frac{1}{2}\overline{[A]}[a][b]\right)+\cdots. \tag{43}$$

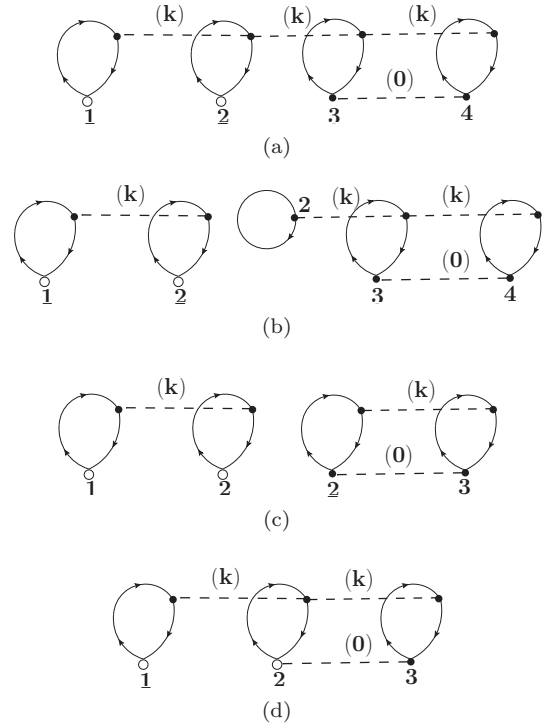

FIG. 7. Examples of diagrams from the families of the first line in Eq. (43).

The terms grouped in each set of parentheses cancel exactly in the classical case and we are left with just $[A]$ the sum of all the connected and nonfactorizable diagrams. In addition, in our quantum case, in many cases of diagrams they also cancel. Figures 7(a) and 7(b) show typical examples of diagrams from sets $\overline{[A\ a]}$ and $\overline{[A]}[a]$, respectively, which cancel each other. The reason for this cancellation is the following. First, the world line of particle 2 in the diagram which comes from $[a]$ in this example is a constant factor, i.e., $L_2(0M)=1/V_\theta$. If we erase this "trivial" world line and replace it by this factor, the two pieces of the diagram of Fig. 7(b) become the pieces of the factorizable diagram of Fig. 7(a) when factorized at point 2. In fact, any diagram from the $\overline{[A\ a]}$ group has a counterpart in the $\overline{[A]}[a]$ group and they mutually cancel. The reverse is not true. Namely, there are diagrams in the $\overline{[A]}[a]$ group which do not have a counterpart in the $\overline{[A\ a]}$ group and they remain. For example, the diagram illustrated in Fig. 7(c) has no counterpart in the $\overline{[A\ a]}$ group, its counterpart is in the $[A]$ group and it is the connected nonfactorizable diagram shown in Fig. 7(d). In the high-temperature limit the diagram

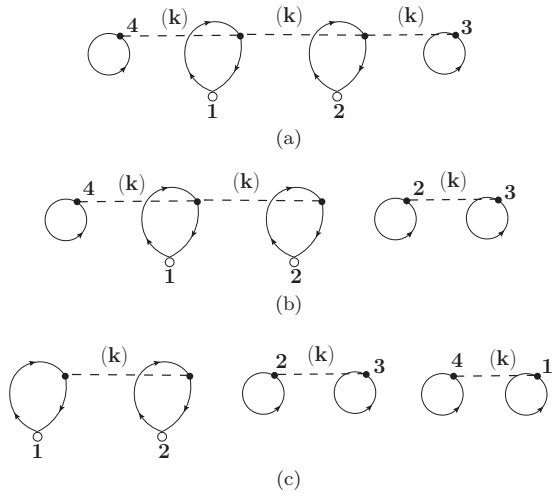

FIG. 8. Example of diagrams from the families of the third line in Eq. (43) with three factorizable parts which cancel.

in Fig. 7(d) becomes factorizable (because the world lines collapse as discussed in the following section) and cancels the diagram in Fig. 7(c). Because pairs of diagrams of this type, such as the two diagrams of Figs. 7(d) and 7(c), nearly cancel at even intermediate temperature we need to either include their contribution together or neglect both.

In general, consider any product of diagrams from the $[\overline{A}][a]$ group. In order to identify its corresponding "partner" diagram in the $[\overline{A\ a}]$ group, we join these disconnected pieces $[A]$ and $[a]$ together at the common particle to create its corresponding factorizable diagram. If the created node is a node of two "nontrivial" world lines, the latter diagram does not exist in the $[\overline{A\ a}]$ group, i.e., as a factorizable diagram at the same point. Again, by a "trivial" world line we mean those in which the corresponding particle has no interactions at any other time slice and, therefore, they have been integrated out, yielding a constant factor of $1/V_\theta$.

In Fig. 8 we give an example of diagrams from the third line in Eq. (43) which cancel each other out. The diagram in Fig. 8(a) is an example from the $[\overline{A\ a\ \ b}]$ group, whereas the diagram in Figs. 8(b) and in 8(c) give its two counterparts which correspond to the families $[\overline{A\ a}][b]$ and $[\overline{A}][a][b]$. These three diagrams together cancel out when we take their prefactors and their symmetry factors into account.

VI. SUMMATION METHODS

As discussed in the previous section, all disconnected diagrams contributing to $g(r)$, which are products of $[A]$ with $[a]$, $[b]$, ..., with common particles, have counterparts in either $[A]$ class or in the class of factorizable diagrams. In addition, we discussed how we can define the partner of any such disconnected diagram. These "paired" diagrams either cancel exactly or they do so in the high-temperature limit. We can neglect the contribution of all such "paired" diagrams at high temperature because their combined contribution is very small. However, for moderately low temperatures these diagrams (examples are shown in Fig. 7) can have finite contribution and hence they must be included.

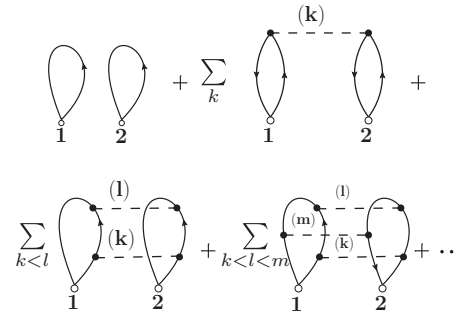

FIG. 9. Expansion of $g(r)$ up to zeroth order in density.

In the next few sections we will explain our summation method and evaluate the distribution function for two distinct sets of systems. One of the systems involves particles interacting with the Lennard-Jones potential

$$v(r) = 4\epsilon\left[\left(\frac{\sigma}{r}\right)^{12} - \left(\frac{\sigma}{r}\right)^{6}\right], \tag{44}$$

as applied to ^{4}He and for particles having the ^{4}He atomic mass (this system has been studied using PIMC simulation [31–35]). The other system involves hard-sphere particles described by the following Hamiltonian:

$$\hat{H} = -\frac{1}{2}\sum_{i=1}^{N}\nabla_i^2 + \sum_{i<j} v(r_{ij}), \tag{45}$$

$$v(r) = \begin{cases} \infty, & r \leqslant 1 \\ 0, & r > 1. \end{cases} \tag{46}$$

The units used here are such that the distance is measured in units of the hard-core radius σ and the energy is measured in units of $\epsilon = \hbar^2/(m\sigma^2)$, where m is the particle mass. There is no energy scale in the classical hard-sphere problem and only the particle density controls the behavior of the pair distribution function. In the quantum mechanical version of the problem [36,37] the kinetic energy operator introduced in the Hamiltonian makes the partition function take the form $Z = tre^{-\theta\hat{H}}$, where $\theta = \epsilon/(k_bT)$. Therefore, the problem is controlled by two parameters, the temperature $\lambda = 1/\theta$ and the particle density. For the case of distinguishable particles, we can obtain exact results for the pair distribution function using the path-integral Monte Carlo method.

A. Density expansion and effective potential

One of the simplest approaches would be to expand $g(r)$ and include all the diagrams up to a certain order in ρ.

(a) *Zeroth order*. The sum of zeroth-order diagrams is given by the infinite series shown in Fig. 9. It is the sum of all possible two-body diagrams which can be obtained by considering all possible ways in which h lines connect the coordinates of these two particles at any time slice.

The sum of these diagrams is needed for two important reasons. We need to sum the entire series in order to obtain the correct behavior in the low-density limit. Second, we need the

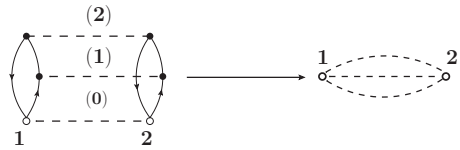

FIG. 10. Collapse of quantum world line in the high-temperature limit. The diagram on the left is also an example of a ladder diagram.

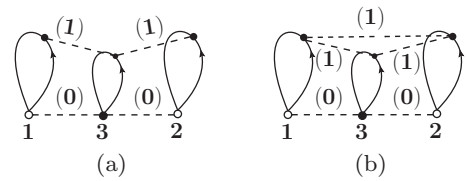

FIG. 12. (a), (b) Examples of first-order (in ρ) ladder diagrams.

entire series in order to obtain the correct classical limit at high temperature. To understand the latter, consider for simplicity the case of fixed number of time slices and the expression for Z given by Eq. (13). When the temperature is high, the world line of any particle collapses to a point: this can be realized mathematically by noticing that the world line is made up of the product of the Gaussians of the form given by Eq. (11) and as the temperature becomes high, $\delta\tau = \hbar\beta/M \to 0$, these Gaussians approach a delta function of the difference in the two positions of the particle at two successive imaginary-time slices. In this case, the integrations over $\vec{r}_i^{(k)}$ for all $k \neq 0$ in Eq. (13) can be carried out. This eliminates all the integrals corresponding to the coordinates $\vec{r}_i^{(k)}$ for $k \neq 0$, and sets $\vec{r}_i^{(k)} = \vec{r}_i^{(0)}$ for $k \neq 0$ in the integrand, thus, Z contains just N integrals over the N-particle coordinates $\vec{r}_i^{(0)}$:

$$\frac{Z}{Z_0} = \int \prod_{n=1}^{N} \frac{d^3 r_n^{(0)}}{V} \prod_{i<j} \left(1 + h_{ij}^{(0)}\right)^M. \tag{47}$$

Notice that, using the definition of $h_{ij}^{(0)}$ [Eq. (10)], the above factor becomes

$$\left(1 + h_{ij}^{(0)}\right)^M = e^{-\beta v(r_{ij}^{(0)})}, \tag{48}$$

i.e., we recover the classical partition function. However, since this product has been expanded to obtain the cluster expansion in the quantum case, i.e.,

$$e^{-\beta v(r_{ij}^{(0)})} = \left(1 + h_{ij}^{(0)}\right)^M = \sum_k \binom{M}{k} \left(h_{ij}^{(0)}\right)^k, \tag{49}$$

it implies that diagrammatically the collapse of the world line leads to multiple h lines connecting any two particles at the coordinates which correspond to the initial time. Figure 10 shows this diagrammatically for the case of $M = 3$.

In Fig. 11 we show the fate of the series of the zeroth-order diagrams of Fig. 9 in the high-temperature limit. This explains the importance of including all zeroth-order diagrams in our formalism. The sum $g_0(r_{12})$ of the zeroth-order diagrams contributing to $g(r)$, i.e., those in Fig. 9, defines an effective

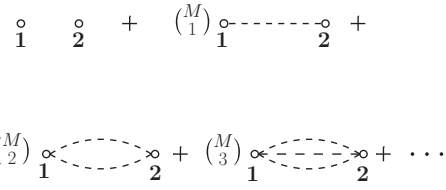

FIG. 11. The fate of the series of the zeroth-order diagrams of Fig. 9 in the high-temperature limit.

potential $v_e(r)$ as follows:

$$g_0(r_{12}) = \exp(-\beta v_e(r_{12})). \tag{50}$$

In order to justify this definition, first, notice that the bare potential is obtained from the high-temperature (classical) and zero-density limit of the distribution function, which is given as

$$\lim_{\beta\to 0} g_0(r_{12}) = \exp\left(-\beta v(r_{12})\right). \tag{51}$$

Also, the high-temperature limit of the sum presented in Fig. 9 is the sum given in Fig. 11. The latter sum is equal to the result given by the above Eq. (51). This implies that in the above definition the effective potential corresponds to the case where instead of freezing the particles' coordinates at their initial values, which would lead to the classical limit, we allow them to fluctuate in imaginary time. In the zero-density limit, there are only the world lines of the two external particles that matter.

The calculation of the sum of all zeroth-order diagrams can be done easily by noting that the diagonal part of the exact two-body density matrix is directly proportional to the sum of all the zeroth-order diagrams in the density expansion of $g(r)$. This is true provided that a sufficiently large number of time slices have been used to find the sum. This sum can be calculated by using the matrix-squaring method [35,38] for the two-body density matrix. The exact two-body density matrix at any temperature can be calculated by starting from the exact two-body density matrix at a very high temperature and then using the matrix-squaring method to obtain the exact density matrix at lower temperature.

(b) *First order and second order*. Unlike the zeroth-order diagrams, the higher-order ladder diagrams for an arbitrary number of time slices are harder to calculate. First-order diagrams contain three particles. Examples of diagrams which are first order in ρ are shown in Fig. 12. Similarly, second-order diagrams contain four particles. In all our second-order calculations we also included the contribution of elementary diagrams. We expect that such an expansion up to first order or second order in ρ will only give accurate results in the low-density regime and also in the high-temperature regime.

We calculated the first- and second-order diagrams using the $v_{\rm eff}(r)$ instead of the bare interaction and made sure that the result had converged with respect to the number of time slices (see Appendix E for discussion). The details of evaluation of all the diagrams have been given in Appendix A. In Figs. 13(a) and 13(b) we compare the $g(r)$ using the density expansion with the converged results of PIMC for large enough M for the Lennard-Jones system. For this system we used both low temperature ($T = 1$) and high temperature ($T = 5$) and the density was fixed at helium density

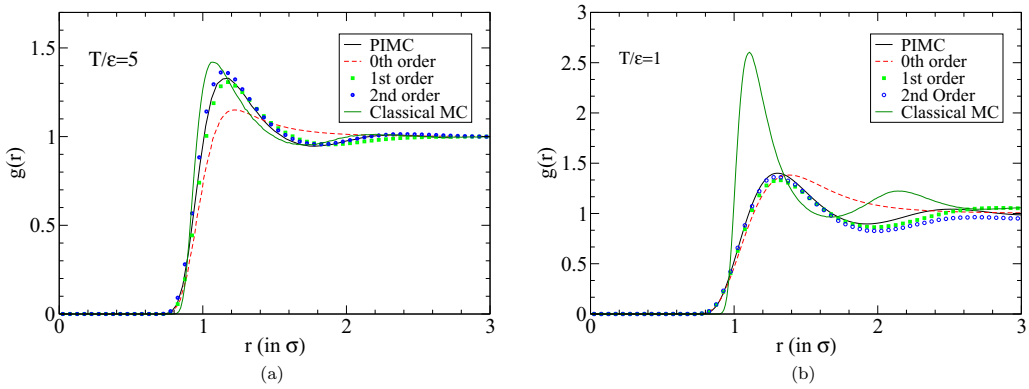

FIG. 13. Comparison of the calculated $g(r)$ within zeroth-order (red dashed line), first-order (green squares), and second-order (blue circles) approximations with the results of our PIMC simulation (black line) for $T/\epsilon = 5$ (a) and $T/\epsilon = 1$ (b) for the Lennard-Jones system. The green solid line is the result of classical Monte Carlo simulation.

$\rho = 0.365\ \sigma^{-3}$. For both temperature values we have included the contribution of the "paired diagrams" mentioned in the beginning of Sec. VI (examples are shown in Fig. 7), and found that they have small contribution at $T = 1$ and negligible contribution at $T = 5$. Since the contribution from first-order "paired diagrams" was small, we ignored the second-order "paired diagrams" in our calculations. In Fig. 14, we compare the distribution function obtained by using the density expansion with the converged results of PIMC for the hard-sphere system. Here, we used two different temperatures, namely, $\lambda = 1$ and 5, and the density was fixed at $\rho = 0.125\sigma^{-3}$. We also included the contribution of the first-order paired diagrams and found their contribution to be negligible for both the temperatures. This also implies that the second-order contribution from the paired diagrams can be ignored for the hard-sphere system. For both the Lennard-Jones and hard-sphere systems, we have also added the results obtained for the same density for the respective classical system.

For both systems, there is a significant difference between the classical MC and the results of PIMC obtained for the quantum case. We can see that the density expansion surprisingly yields results for the pair distribution function which, in general, agree with the PIMC results at smaller distances at both low and high temperatures. As expected, the agreement with PIMC is better when the temperature is high. We also notice that for lower temperature the density expansion is unable to correctly capture the long-range part of the distribution function. For cases with low density or high temperature, including first few orders of term may be sufficient to yield accurate results but the same is not true when temperature is low or density is high. In the next section, we will discuss the Padé approximation scheme, which can produce results with improved agreement with PIMC simulation.

B. Padé approximation

In the previous sections we discussed the series expansion of the pair distribution function up to a given order m, i.e.,

$$g^{(m)}(r_{12}) = \sum_{n=0}^{m} g_n(r_{12}), \tag{52}$$

where $g_n(r_{12}) = d_n(r_{12})\rho^n$, i.e., it is the sum of all diagrams which include n internal particles and they are of order of ρ^n.

It is a common practice in various expansion techniques, such as high-temperature series expansion, to use Padé approximants as an extrapolation tool in conjunction with

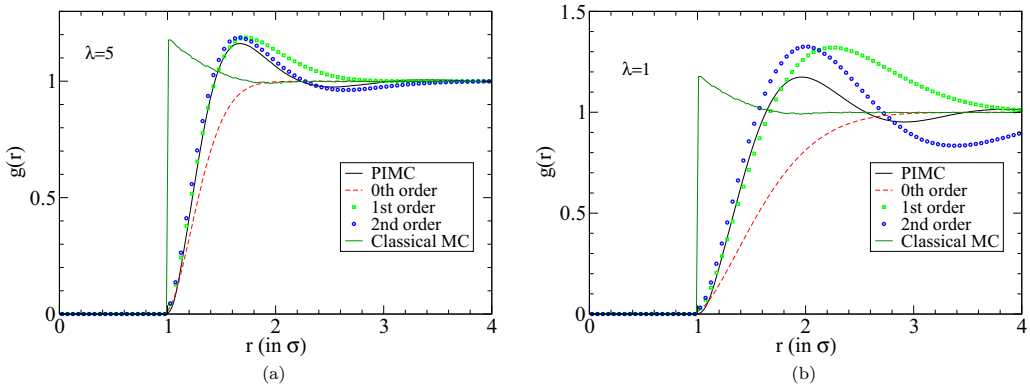

FIG. 14. Comparison of the calculated pair distribution function within zeroth-order (red dashed line), first-order (green squares), and second-order (blue circles) approximations with the result of our PIMC simulation (black line) for the hard-sphere system. The green solid line represents the result of classical Monte Carlo simulation. In (a) the value of λ is 5 and in (b) the value of λ is 1. The density used is 0.125 (in units of σ^{-3}).

information obtained from calculating the observable quantity up to a given order in the expansion parameter. As we noticed in the calculation of $g(r)$, the order-by-order expansion is more accurate at small distances and progressively fails as the distance is increased. This can be easily understood by the fact that the n-body clusters included miss the higher-order nodal diagrams which are convolutions of longer chains of many particles. By working in momentum space, however, and using Padé approximants, as shown below, captures the contribution of these terms.

We consider the diagrammatic expansion of the Fourier transform of $g(r)-1$, i.e., of $S(k)-1$, defined as

$$S(k)-1=\rho\int d^3r[g(r)-1]e^{i\vec{k}\cdot\vec{r}}\equiv\rho\Delta(k). \tag{53}$$

The most general form of the Padé approximant for $\Delta(k)$ is given by

$$\Delta(k)=\frac{a_0+a_1\rho+a_2\rho^2+\cdots}{1+b_1\rho+b_2\rho^2+\cdots}. \tag{54}$$

The coefficients a_n and b_n can be determined by expanding the above expression in power of ρ and equating the coefficients of the expansion to those obtained by order-by-order expansion in the previous section. Below we mention some equations for the first few values of n:

$$\begin{bmatrix}\tilde{g}_0\\ \tilde{g}_1\\ \tilde{g}_2\end{bmatrix}=\begin{bmatrix}a_0\\ a_1-a_0b_1\\ a_2-b_2a_0-b_1a_1+b_1^2a_0\end{bmatrix}, \tag{55}$$

where $\tilde{g}_0$, $\tilde{g}_1$, and $\tilde{g}_2$ are the Fourier transforms of $d_0(r_{12})-1$, $d_1(r_{12})$, and $d_2(r_{12})$, respectively. Although a_0 is uniquely determined, there is only one equation relating a_n and b_n and, therefore, we need another constraint to determine both unknowns. This additional constraint needed is obtained by requiring the Padé expansion to yield the exact high-temperature limit of the distribution function (i.e., the classical limit). This is discussed next.

We begin by noticing that for the classical system $g(r)-1$ is given by

$$g_c(r)-1=N(r)+X(r), \tag{56}$$

where $X(r)$ represents the composite diagrams and $N(r)$ represents the nodal diagrams. The Fourier transform of the above equation becomes

$$\Delta_c(k)=\widetilde{X}(k)+\widetilde{N}(k). \tag{57}$$

The nodal diagrams are related to the non-nodal diagrams through a Dyson-type equation which is the so-called HNC equation which in momentum space can be written as follows:

$$\tilde{N}(k)=\frac{\rho\tilde{X}^2(k)}{1-\rho\tilde{X}(k)}. \tag{58}$$

Notice that this is an exact relationship and the HNC becomes an approximation when one neglects the contribution of the elementary diagrams. We have no need to proceed to such an approximation here.

Combining the above two equations we obtain

$$\Delta_c(k)=\frac{\tilde{X}(k)}{1-\rho\tilde{X}(k)}. \tag{59}$$

Next, we write the $\tilde{X}$ as follows:

$$\tilde{X}(k)=A_0+A_1\rho+A_2\rho^2+\cdots. \tag{60}$$

Substituting $\tilde{X}(k)$ into our previous equation for $\Delta_c(k)$ we find that

$$\Delta_c(k)=\frac{A_0+A_1\rho+A_2\rho^2+\cdots}{1-\rho(A_0+A_1\rho+A_2\rho^2+\cdots)}. \tag{61}$$

We demand that Eq. (54) in the high-temperature limit becomes Eq. (61). This yields the following:

$$\lim_{T\to\infty}a_n=A_n, \tag{62}$$

$$\lim_{T\to\infty}b_n=-A_{n-1}(\forall\, n\geqslant 1). \tag{63}$$

First, it can be easily shown that all the a_n coefficients in the expression for $\Delta(k)$ in the quantum case [Eq. (54)] in the high-temperature limit become equal to A_n in Eq. (61). This is shown in Appendix B. Furthermore, we will enforce the constraint

$$b_n=-a_{n-1}\,(\forall\, n\geqslant 1) \tag{64}$$

for the coefficients of our Padé approximants in Eq. (54) for any temperature [which should be satisfied in the high-temperature limit according to Eq. (63)]. Using this constraint relating the coefficients of the numerator with those of the denominator of Eqs. (54) and (55) the coefficients of the Padé approximants of our quantum case can be determined uniquely from the power-series expansion in density ρ discussed in the previous section.

In Fig. 15(a) we show the results of the density expansion and the results obtained by using the Padé approximation using the first-order calculation of the coefficients of the expansion in ρ. As can be inferred from the figure, the density expansion is more accurate at short distances and the Padé is more accurate at long distances as expected. This was discussed in the beginning of this section as the motivation for carrying out the Padé approximation. Therefore, it seems reasonable to use density expansion for the short-range part of the distribution function and the Padé for its long-range part. This means that up to some distance r_0 the distribution function will be evaluated by using the density expansion and beyond r_0 it will be determined by using Padé approximants. A detailed description of the procedure to identify r_0 and the interpolation between the two parts is discussed in Appendix C. In Fig. 15(b) the result of joining these two parts of the distribution function (calculated by using the coefficients of the density in first-order density expansion) is compared with the exact obtained by means of PIMC.

In Fig. 16 we show the full distribution function obtained by using different orders of Padé approximation in conjunction with the density expansion for the same system. Clearly, the results improve as we go from the first-order Padé to the second-order Padé approximation. We also note that the region around the first peak and beyond is more accurate when compared against the results from the density expansion. The improvement in the long-range part of $g(r)$ is the reason for using Padé in momentum space as discussed earlier.

A simple test of our method is to compare the results for the distribution function for a classical system with those obtained

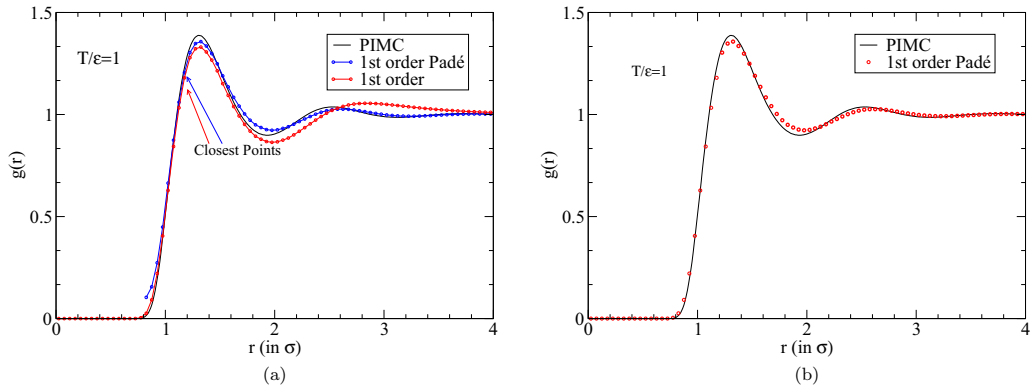

FIG. 15. Comparison of $g(r)$ for particles interacting with Lennard-Jones potential for density $\rho = 0.365\sigma^{-3}$ and for temperature $T/\epsilon = 1$. In (a) the solid blue line with points is the result obtained from first-order Padé approximation $[g^p(r)]$ and the solid red line with points is the the result obtained by summing all diagrams up to first order in density $[g^{(1)}(r)]$. In (b) we present the final result (red circles) after combining the $g^{(1)}(r)$ and $g^p(r)$ curves and comparing it against PIMC simulation (solid black line).

by Monte Carlo. The classical limit is obtained from the Feynman path integral with no time slice in the interval $[0, \hbar\beta]$ and our results, obtained using up to second-order cluster expansion followed by Padé approximants to extrapolate to infinite order, are discussed in Appendix D. The conclusion of this comparison is that even by restricting ourselves to just second order, the results are very close to the Monte Carlo results, and they systematically improve by increasing the order of the expansion.

In Fig. 17, we present the results using Padé approximation for the hard-sphere system. The short-range part of the distribution function was once again obtained by the density expansion. The results become more accurate once we transition from the first-order Padé to the second-order Padé approximation. In the $\lambda = 1$ case, the naive density expansion up to second order fails to yield accurate results, whereas the second-order Padé produces a $g(r)$ close to PIMC simulation [see Figs. 14(b) and 17(b)]. For the $\lambda = 5$ case, the second-order density expansion is already in close agreement with the PIMC simulation and the second-order Padé improves this agreement even further [see Figs. 14(a) and 17(a)].

VII. FUTURE DIRECTIONS: INCLUDING EXCHANGES

In this paper we have successfully applied the idea of cluster expansion to the case of interacting distinguishable particles with significant quantum effects. We can generalize this approach to the case of identical particles and, in particular, to fermions. This means including all diagrams with exchanges contributing to our equations for the zeroth-, first-, and second-order expansions. We would like to emphasize that adding exchange diagrams order by order to the distinguishable particle distribution function is not going to capture the Fermi-liquid behavior of the system. This is because the full Fermi- or Bose-liquid behavior can only be captured correctly once exchange diagrams of all orders have been included. However, in the temperature regimes which are only able to facilitate two or three particle exchanges, one can safely assume that the system is predominantly in the phase where they can be considered as distinguishable. In such situations, the approach of adding zeroth- or first-order exchange diagrams as corrections to the distinguishable particle distribution function can be effective. The set of all

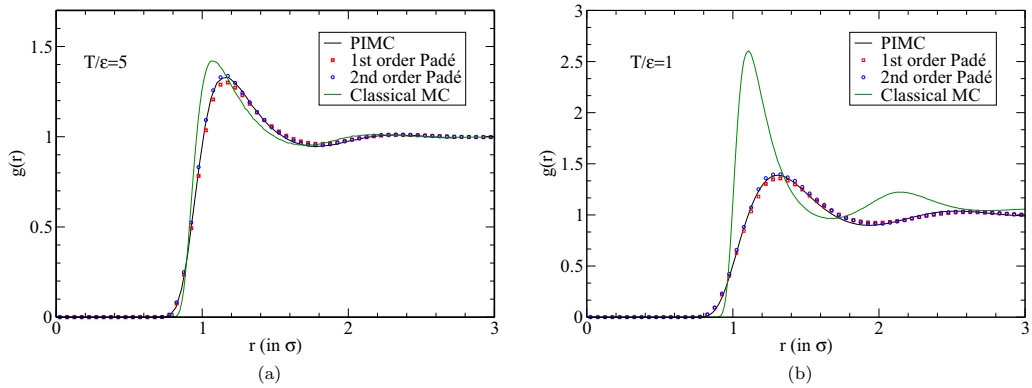

FIG. 16. Comparison of $g(r)$ for particles interacting with Lennard-Jones potential for density $\rho = 0.365\sigma^{-3}$ and for temperature (a) $T/\epsilon = 5$ and (b) $T/\epsilon = 1$. The black solid line is the result obtained from our PIMC simulation extrapolated to $M \to \infty$ and $N \to \infty$. The green solid line is the result from classical Monte Carlo. The red squares and blue circles represent the results obtained by first- and second-order Padé approximation, respectively. The short-range part of the first- (second-) order Padé was obtained by the first- (second-) order density expansion using the procedure described in Sec. VI B.

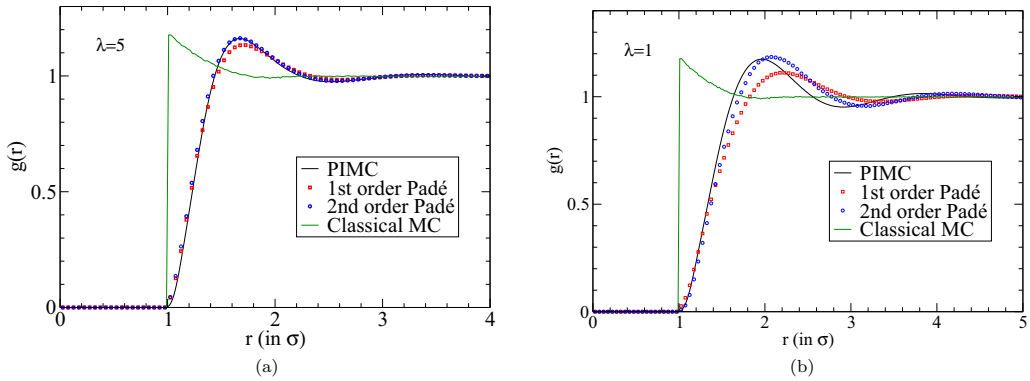

FIG. 17. Comparison of the calculated pair distribution function with first-order Padé (red squares) and second-order Padé (blue circles) approximations with the result of our PIMC simulation (black line) for hard-sphere system. The short-range part of the first- (second-) order Padé was obtained by the first- (second-) order density expansion using the procedure described in Sec. VI B. In (a) the value of λ is 5 and in (b) the value of λ is 1. The density used is 0.125 (in units of σ^{-3}).

zeroth-order exchange diagrams are shown in Fig. 18. There are exactly 2^M distinct zeroth-order exchange diagrams when using M time slices for the Trotter approximation, however, all of them can be included by carrying the matrix-squaring technique adopted in this paper. In Fig. 19 we show some examples of three-body (first-order) and four-body (second-order) exchange diagrams. There are $4 \times 8^M - 3 \times 2^M$ three-body exchange diagrams for the case of M time slices. They can be included and it is a part of our next project.

For the case of fermions, the terms corresponding to all the zeroth-order diagrams shown in Fig. 18 have a negative contribution (as only one exchange takes place). In a similar way, the terms corresponding to Fig. 19(b) have positive contribution (as there are two exchanges). Since our method is not stochastic in nature it does not suffer from these negative contributions which present a problem for QMC. In our future work we plan to implement this method for the case of fermions and to compare the result with those obtained by approximate QMC methods, such as the fixed-node approximation.

VIII. SUMMARY OF IMPLEMENTATION

The calculation of an observable is written as a series expansion in powers of the particle density ρ. In the case where we are interested in the pair-distribution function $g(r)$, which is the main subject of this paper, the series up to the m

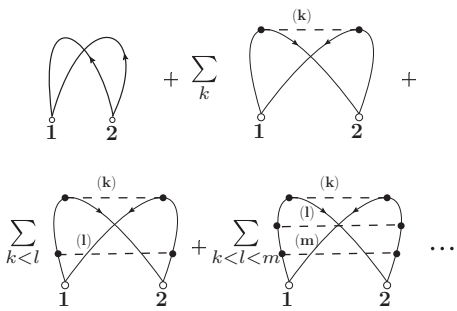

FIG. 18. The sum of all zeroth-order exchange diagrams for M time slices.

order is written as

$$g^{(m)}(r_{12}) = \sum_{n=0}^{m} g_n(r_{12}), \tag{65}$$

where $g_n(r_{12})$ contains a factor of ρ^n. Any term contributing to $g(r)$ is represented by a diagram and the diagrammatic rules are specified in Secs. III and V. Any such diagram involves $n+2$ particles, two of which are external points (open circles) and the other n particles represent internal points (solid circles) which are integration variables. For each such internal particle there is a density factor associated with it. Therefore, an $(n+2)$-body diagram is a ρ^n-order term.

(i) The first step is to specify the maximum order m up to which the distribution function is to be evaluated. The nth-order contribution refers to including all diagrams which contain $n+2$ particles. In this paper we have included the case where $m = 2$. In addition, one needs to choose the number of time slices M that is going to be used.

(ii) Next, one should use the diagrammatic rules discussed in Secs. III and V to find and evaluate all the diagrams up to the specified order for the chosen number of time slices M. The zeroth order contains all diagrams with two particles (which would be the external particles), the first order contains all diagrams with three particles, and the second order includes all diagrams with four particles, etc. The diagrams contributing up to the second order and how to find them are discussed in Sec. VI in detail.

(iii) Each diagram is an integral which can be calculated numerically or when it involves many time slices using the Monte Carlo integration method. In Appendix A we give the general expression to use to evaluate all the zeroth- $[g_0(r_{12})]$, first- $[g_1(r_{12})]$, and second-order $[g_2(r_{12})]$ diagrams.

(iv) The previous three steps should be repeated by increasing the number of time slices M keeping the maximum order of expansion m fixed. The calculation is complete when convergence is achieved with respect to the number of time slices M.

This approach can provide accurate results in the low-density and/or in the high-temperature regime. For more accurate results we carry out the following additional steps.

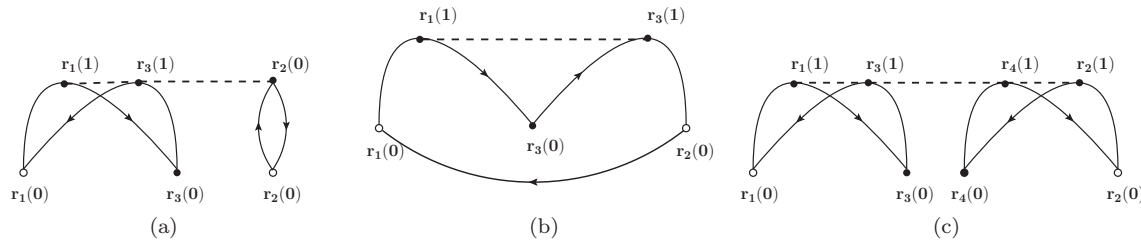

FIG. 19. (a) Example of first-order exchange diagram involving a single two-particle exchange. (b) Example of another first-order exchange diagram with a three-particle exchange. (c) Example of second-order exchange diagram involving two two-particle exchanges.

(1) Next, we obtain an extrapolation to infinite order $g^p(r)$ by using Padé approximants, as it is customary in other expansion methods. As usual, the coefficients of the Padé approximants are determined in such a way to yield the same order-by-order expansion, as in Eq. (65), up to the calculated order. In addition, the form of the Padé expression is required to yield the exact high-temperature limit. How to do that is explained in detail in Sec. VI B.

(2) The pair distribution function $g^p(r)$ obtained by using Padé is more (less) accurate than $g^{(m)}(r)$ obtained by density expansion at larger (smaller) distances. As discussed in Sec. VI B, $g^{(m)}(r)$ accurately captures the short-range part of the distribution function and $g^p(r)$ is more accurate at larger distances. Therefore, the full distribution function can be constructed by combining the two results using the procedure described in Sec. VI B and Appendix C.

IX. CONCLUSIONS

We have revived the old well-known method of cluster expansion and virial expansion in classical statistical mechanics [16] by extending its application to the many-body path integral and we have derived a diagrammatic expansion for the free energy and the pair distribution function. The series expansion which can be written as a formal power-series expansion in the particle density ρ can be also thought of as an expansion where we keep all diagrams involving up to n-body linked clusters. We provide a complete formalism and the diagrammatic rules so one can systematically calculate the free energy and the distribution function in a order-by-order approach or by developing resummation techniques in the future to include the most significant contribution of the terms of the series.

We have also attempted to demonstrate the rather fast convergence of the approach with respect to the order n and we used Padé approximants to extrapolate to infinite order. We benchmarked the method by applying it to problems of strongly correlated distinguishable particles because in this case we can compare our results to those we obtained by using the PIMC technique which is exact for distinguishable particles. We carry out calculations of $g(r)$ by including up to three-body diagrams (first order in ρ) and up to four-body diagrams (second order in ρ) for both Lennard-Jones and the hard-sphere problem for high densities and moderately low temperature. The results are in good agreement with those obtained by PIMC while the long-distance behavior is not satisfactorily accurate because a finite order does not include long-range correlations arising from multiparticle chain diagrams.

Working in momentum space, we introduce a standard Padé approximation scheme, however, constrained to exactly reproduce the nth-order expansion obtained from the cluster expansion and to yield the exact results in the high-temperature classical limit. This extension gives a good agreement with the exact results obtained with PIMC both for the Lennard-Jones and hard-sphere problem.

We have shown that our method is formally generalizable to the case of identical particles and in particular to the case of fermions by adding a finite number of exchange diagrams to every order of our expansion. This is a similar situation to the well-known perturbation theory for fermions [1]. We hope that this method can provide useful results when applied to practical problems of interacting Fermi systems. If so, the results can be used to compare with the results obtained by applying quantum Monte Carlo (QMC) methods in this latter case. Our method is simple but tedious and time consuming and we hope to provide results for this case in the near future.

We would also like to add that the approach of keeping just the n-body clusters, which works very well for the distinguishable particle case, when employed for Bose or Fermi systems should give a reasonable account of the contribution of particle permutations when inside the Mott phase. In our formulation, the so-called Mott-insulator phase occurs when particle exchanges are exponentially suppressed because of increased localization. As long as we stay not too close to the boundary between the Mott insulator and the Fermi-liquid phase, the contribution of the particle exchanges can be included in our n-body cluster calculation as outlined in Sec. VII. However, in order to obtain the full Fermi- or Bose-liquid behavior, one must include diagrams with long chains of particle exchange, which is a difficult task to achieve with our method. The method of keeping n-body clusters can also work in the temperature regime which allows only for few particle exchanges. Notice that for liquid ^{4}He multiparticle exchanges start contributing to the PIMC simulation only very close to the superfluid transition temperature [39].

ACKNOWLEDGMENTS

This work was supported in part by the U. S. National High Magnetic Field Laboratory, which is funded by NSF Grant No. DMR-1644779 and the State of Florida.

APPENDIX A: CALCULATION OF DIAGRAMS

We first define a generalized H line given by the following expression:

$$H_{12} = \prod_{k=0}^{M-1}\left(1 + h_{12}^{(k)}\right) - 1. \tag{A1}$$

With the assumption that the external points are at $r_1^{(0)}$ and $r_2^{(0)}$, the sum of all zeroth-order diagrams [given by $g_0(r_{12}^{(0)})$] can be determined using the following expression:

$$g_0\left(r_{12}^{(0)}\right) = V_\theta^2 \int \prod_{n=1}^{2}\prod_{k=0}^{M-1} L_n(kk+1) \prod_{n=1}^{2}\prod_{k=1}^{M-1} d^3 r_n^{(k)} (1 + H_{12}). \tag{A2}$$

In a similar way, the sum of all first-order diagrams [denoted by $g_1(r_{12}^{(0)})$] can be evaluated using the following expression:

$$g_1\left(r_{12}^{(0)}\right) = \rho V_\theta^3 \int \prod_{n=1}^{3}\prod_{k=0}^{M-1} L_n(kk+1)(1 + H_{12}) H_{13} H_{32} \times \prod_{n=1}^{2}\prod_{k=1}^{M-1} d^3 r_n^{(k)} \prod_{k=0}^{M-1} d^3 r_3^{(k)}. \tag{A3}$$

The expression above does not include the first-order "paired" diagrams. In a similar way, the sum of all second-order diagrams [denoted by $g_2(r_{12}^{(0)})$] can be evaluated using the following expression:

$$g_2\left(r_{12}^{(0)}\right) = \rho^2 V_\theta^4 \int \prod_{n=1}^{4}\prod_{k=0}^{M-1} L_n(kk+1)(1 + H_{12}) H_{13} H_{42} \times \left[H_{34}\left(1 + H_{14} + H_{32} + \frac{H_{14}H_{32}}{2}\right) + \frac{H_{32}H_{14}}{2}\right] \times \prod_{n=1}^{4}\prod_{k=1}^{M-1} d^3 r_n^{(k)} d^3 r_3^{(0)} d^3 r_4^{(0)}. \tag{A4}$$

The expression for the second-order diagrams also includes the elementary diagrams. The integrals mentioned above have been calculated using Monte Carlo integration method.

APPENDIX B: HIGH-TEMPERATURE LIMIT OF THE PADÉ APPROXIMATION

At the zeroth-order level of approximation ($a_0 = \tilde{g}_0$) the $\Delta(k)$ is given by

$$\Delta(k) = \frac{\tilde{g}_0(k)}{1 - \rho\tilde{g}_0(k)}. \tag{B1}$$

As a reminder, the $\tilde{g}_0(k)$ is the Fourier transform of $g_0(r_{12}) - 1$ which is calculated using the zeroth-order quantum diagrams shown in Fig. 9. When we take the high-temperature limit, all the world lines shown in the figure collapse and $\tilde{g}_0$ becomes exactly equal to the Fourier transform of the classical h line ($\tilde{h}_{cl}$). This means that Eq. (B1) in the high-temperature limit yields the exact same result as Eq. (59) with $\tilde{X}$ substituted by $\tilde{h}_{cl}$. When we move to the first-order approximation for Eq. (54) and use Eq. (63) we obtain

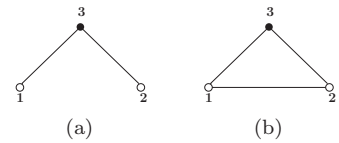

FIG. 20. (a), (b) Represent the first-order classical nodal and composite diagrams, respectively. The solid line here represents the classical h line.

$$\Delta(k) = \frac{\tilde{g}_0(k) + \rho a_1(k)}{1 - \rho[\tilde{g}_0(k) + \rho a_1(k)]}, \tag{B2}$$

where the value of a_1 is obtained from the equation

$$a_1 = \tilde{g}_1 - \tilde{g}_0\tilde{g}_0. \tag{B3}$$

In the real space, the last term in the previous equation is a convolution of g_0 with itself. In the high-temperature limit, this term should clearly approach the first-order classical nodal diagram shown in Fig. 20(a) (as $\tilde{g}_0 \to \tilde{h}_{cl}$). Since $\tilde{g}_1$ becomes the classical first-order diagram (g_1^c) and $\tilde{g}_0^2$ becomes the classical first-order nodal diagrams in the high-temperature limit, a_1 becomes the classical composite diagram [shown in Fig. 20(b)] in the high-temperature limit thereby successfully satisfying our constraint. Using similar reasoning, one can show that the equality between the high-temperature limit of Eq. (54) and its classical counterpart [Eq. (59)] is not just limited to zeroth- or first-order approximations but extends to any order of approximation.

APPENDIX C: COMBINING THE DENSITY EXPANSION AND PADÉ APPROXIMATION

In this Appendix we have highlighted the main steps to identify the distance r_0 which serves as a connection point for the results obtained by density expansion and Padé approximation. Once the r_0 has been identified, the pair distribution function near the region $r\epsilon(r_0 - \delta r, r_0 + \delta r)$ is determined by interpolation (this makes sure that the final distribution function is not discontinuous). Everywhere else the distribution function is given by the following:

$$g(r) = \begin{cases} g^{(m)}(r), & r \leqslant r_0 - \delta r \\ g^p(r), & r \geqslant r_0 + \delta r. \end{cases} \tag{C1}$$

Here, $g^{(m)}(r)$ and $g^p(r)$ represent the distribution function obtained by density expansion and Padé approximation, respectively. Since we work with discretized values for distances in computer simulation, the value of δr can be chosen to be the mesh size. For our case, the value of the distribution function at distance r_0 was chosen to be the average of $g^{(m)}(r_0)$ and $g^p(r_0)$. It can be easily shown that using the average is equivalent to using a quadratic polynomial $[f(r)]$ for interpolation with the constraint

$$f(r) = \begin{cases} g^{(m)}(r), & r = r_0 - \delta r \\ g^p(r), & r = r_0 + \delta r. \end{cases} \tag{C2}$$

Below we have described the procedure that we have used to choose the r_0:

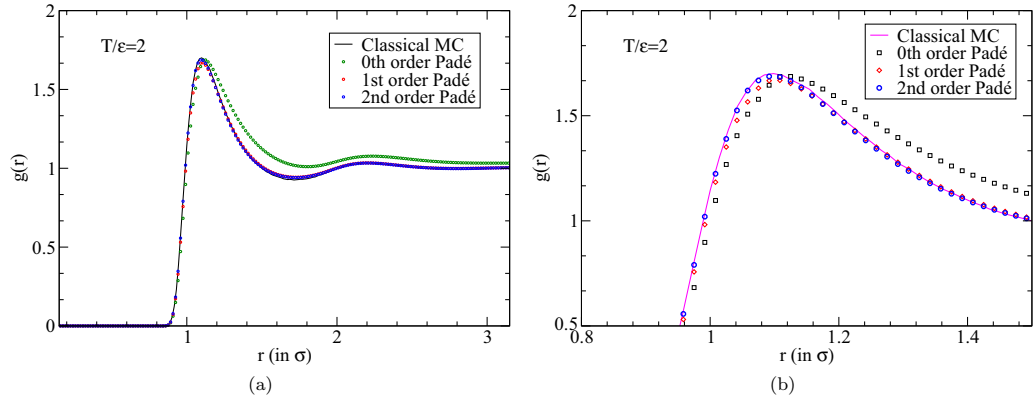

FIG. 21. (a) Shows comparison of the calculated pair distribution function with zeroth- (green circles), first- (red circles), and second- (blue circles) order Padé approximation with the result of our classical MC simulation (black line) for a classical Lennard-Jones system. The short-range part of the zeroth-/first-/second-order Padé was obtained from the zeroth-/first-/second-order density expansion using the procedure described in Sec. VI B. (b) Focuses on the region around the peak shown in (a). The value of temperature used is 2 (in units of ϵ) and that of density used is 0.365 (in units of σ^{-3}).

(i) If the two distribution functions intersect or touch each other before the location of the first peak of the distribution function, then that point can be designated as the r_0.

(ii) If the two distribution functions do not intersect, then we identify r_0 as the x coordinate of the data points on $g^{(m)}$ and g^p curve that are closest to each other. The only restriction being that the location of r_0 must be before the location of the first peak of the distribution function.

In Fig. 15 we demonstrate how one can construct the full distribution function using the $g^{(m)}$ and g^p curves for a Lennard-Jones system.

APPENDIX D: PADÉ APPROXIMATION FOR CLASSICAL SYSTEM

We applied the Padé approximation scheme to obtain the pair distribution function for a classical Lennard-Jones system. We begin by assuming that $X_0(r)$, $X_1(r)$, and $X_2(r)$ represent the zeroth-, first-, and second-order composite diagrams for the classical system. The Padé approximation for the classical system can be performed by using Eq. (61) where A_0, A_1, and A_2 are the Fourier transforms of $X_0(r)$, $\rho^{-1}X_1(r)$, and $\rho^{-2}X_2(r)$, respectively. The density (ρ) used was 0.365 σ^{-3} and the temperature was 2 (in units of ϵ). The results obtained from different orders of Padé approximations have been compared against the result obtained from the classical MC in Fig. 21(a). The short-range part of the distribution function was once again obtained by using density expansion. Both Figs. 21(a) and 21(b) show the same result with the latter focusing around the region near the peak and clearly demonstrating how the result improves as we include higher-order terms.

APPENDIX E: CONVERGENCE OF DIAGRAMS WITH RESPECT TO THE NUMBER OF TIME SLICES M

The Trotter approximation is only valid in the limit $M \to \infty$. Since we work only with finite number of time slices, we demonstrate that we have reached the $M \to \infty$ limit by showing that our results have converged with respect to the number of time slices. In this Appendix we show the variation of both zeroth-order and first-order diagrams with respect to

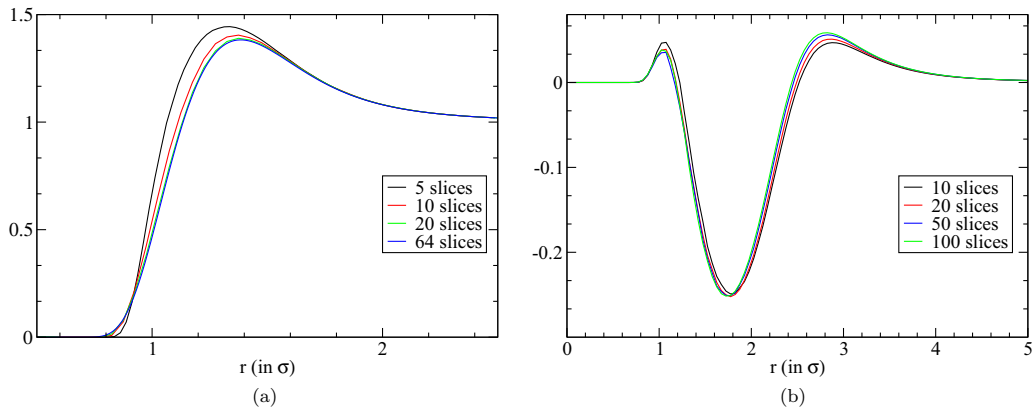

FIG. 22. (a) Variation of different orders of diagrams with respect to number of time slices for a Lennard-Jones system at $T/\epsilon = 1$ and $\rho = 0.365\sigma^{-3}$. (a) Shows zeroth-order diagrams calculated using different time slices starting from the bare Lennard-Jones interaction. (b) Shows first-order diagrams calculated using different time slices using the effective interaction.

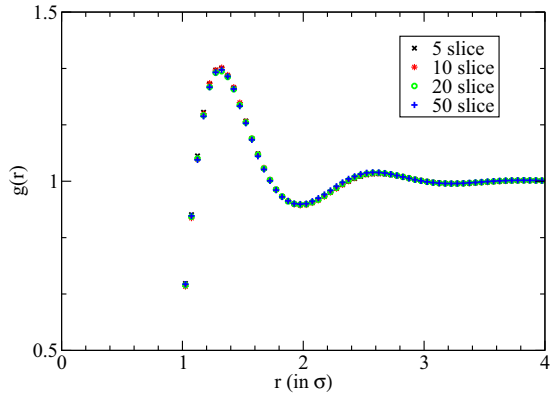

FIG. 23. Convergence of $g^p(r)$ (obtained by using first-order Padé approximation) with the number of time slices M obtained at $\rho = 0.365\sigma^{-3}$ and $T/\epsilon = 1$ for Lennard-Jones system using effective interaction.

the number of time slices. For the purpose of demonstration we consider the Lennard-Jones system at $T/\epsilon = 1$ and $\rho = 0.365\sigma^{-3}$. In Fig. 22(a) we show the variation of zeroth-order diagrams with respect to the number of time slices. It is clear that 20 time slices are sufficient to reach the final converged result. In a similar way, we show in Fig. 22(b) the variation of first-order diagrams with different time slices. It is clear from the figure that the difference between any two first-order diagrams calculated using different number of time slices is small compared to the pair distribution function obtained by summing all clusters up to three-body.

In Fig. 23 we illustrate the convergence of the first-order Padé approximation with respect to the number of time slices for the Lennard-Jones potential. We first made sure that the calculated zeroth-order diagrams have converged with respect to the number of time slices. Next, we used the effective interaction and calculated the first-order diagrams using 5, 10, 20, and 50 time slices. The results were then used along with the converged result of zeroth-order diagrams to obtain the distribution function $g^p(r)$ from the Padé approximation. In the figure we can see that the final results for the different number of time slices are very close to each other.

[1] A. Fetter and J. Walecka, *Quantum Theory of Many-Particle Systems*, Dover Books on Physics (Dover, New York, 2003).
[2] G. Mahan, *Many-Particle Physics*, Physics of Solids and Liquids (Springer, New York, 1990).
[3] A. Abrikosov, L. Gorkov, I. Dzyaloshinski, and R. Silverman, *Methods of Quantum Field Theory in Statistical Physics*, Dover Books on Physics (Dover, New York, 2012).
[4] R. Feynman, *Statistical Mechanics: A Set Of Lectures*, Advanced Books Classics (CRC Press, Boca Raton, FL, 1998).
[5] J. Negele and H. Orland, *Quantum Many-Particle Systems*, Frontiers in Physics (CRC Press, Boca Raton, FL, 1988).
[6] H. Bethe and E. Salpeter, Phys. Rev. **84**, 1232 (1951).
[7] V. M. Galitskii, Zh. Eksp. Teor. Fiz. **34**, 151 (1958) [J. Exp. Theor. Phys. **7**, 104 (1958)].
[8] E. Wigner, Phys. Rev. **40**, 749 (1932).
[9] J.-P. Hansen and J.-J. Weis, Phys. Rev. **188**, 314 (1969).
[10] F. Barocchi, M. Moraldi, and M. Zoppi, Phys. Rev. A **26**, 2168 (1982).
[11] F. Barocchi, M. Zoppi, and M. Neumann, Phys. Rev. A **27**, 1587 (1983).
[12] F. Barocchi, M. Neumann, and M. Zoppi, Phys. Rev. A **29**, 1331 (1984).
[13] F. Barocchi, M. Neumann, and M. Zoppi, Phys. Rev. A **31**, 4015 (1985).
[14] F. Barocchi, M. Neumann, and M. Zoppi, Phys. Rev. A **36**, 2440 (1987).
[15] R. P. Feynman and A. R. Hibbs, *Quantum Mechanics and Path Integrals* (McGraw-Hill, New York, 1965).
[16] J. E. Mayer and M. G. Mayer, *Statistical Mechanics* (Wiley, New York, 1940), Chap. 13.
[17] D. Goodstein, *States of Matter*, Dover Books on Physics Series (Dover, New York, 2002).
[18] K. Hiroike, J. Phys. Soc. Jpn **12**, 326 (1957).
[19] K. Hiroike, J. Phys. Soc. Jpn **12**, 864 (1957).
[20] T. Morita, Prog. Theor. Phys. **20**, 920 (1958).
[21] T. Morita, Prog. Theor. Phys. **21**, 361 (1959).
[22] T. Morita, Prog. Theor. Phys. **23**, 175 (1960).
[23] T. Morita, Prog. Theor. Phys. **23**, 829 (1960).
[24] T. Morita and K. Hiroike, Prog. Theor. Phys. **23**, 1003 (1960).
[25] R. R. P. Singh, Phys. Rev. B **39**, 9760 (1989).
[26] R. Shankar and G. Murthy, Phys. Lett. A **137**, 165 (1989).
[27] R. R. P. Singh, P. A. Fleury, K. B. Lyons, and P. E. Sulewski, Phys. Rev. Lett. **62**, 2736 (1989).
[28] V. R. Pandharipande and R. B. Wiringa, Rev. Mod. Phys. **51**, 821 (1979).
[29] S. Fantoni and S. Rosati, Il Nuovo Cimento A **25**, 593 (1975).
[30] E. Manousakis, S. Fantoni, V. R. Pandharipande, and Q. N. Usmani, Phys. Rev. B **28**, 3770 (1983).
[31] E. L. Pollock and D. M. Ceperley, Phys. Rev. B **30**, 2555 (1984).
[32] D. M. Ceperley and E. L. Pollock, Phys. Rev. Lett. **56**, 351 (1986).
[33] E. L. Pollock and D. M. Ceperley, Phys. Rev. B **36**, 8343 (1987).
[34] D. M. Ceperley and E. L. Pollock, Phys. Rev. B **39**, 2084 (1989).
[35] D. M. Ceperley and E. L. Pollock, in *Monte Carlo Methods in Theoretical Physics*, edited by S. Caracciolo and A. Fabrocini (ETS Edtrice, Pisa, Italy, 1992), p. 35.
[36] K. J. Runge and G. V. Chester, Phys. Rev. B **38**, 135 (1988).
[37] M. H. Kalos, D. Levesque, and L. Verlet, Phys. Rev. A **9**, 2178 (1974).
[38] A. Klemm and R. Storer, Aust. J. Phys. **26**, 43 (1973).
[39] D. M. Ceperley, Rev. Mod. Phys. **67**, 279 (1995).